



Cite this: *Phys. Chem. Chem. Phys.*,
2018, 20, 19995

Epitaxial 8YSZ/Y₂Zr₂O₇ multilayers: a conductivity and strain study

Elisa Gilardi, *† Giuliano Gregori and Joachim Maier 

Thin films of Y₂Zr₂O₇ were grown *via* pulsed laser deposition (PLD) on substrates of MgO(110), Al₂O₃(0001) and Al₂O₃(1102). Electrical properties were investigated *via* electrical impedance spectroscopy. Unexpectedly, the ionic conductivity is not affected by the microstructure; only minor differences in conductivities and activation energies were measured between epitaxial thin films (on MgO) and textured thin films (on Al₂O₃, both orientations). This indicates the grain boundaries of such a material to only marginally block the oxygen vacancy transport. Starting from these results, epitaxial multilayers of Y₂Zr₂O₇ and 8 mol% yttria-stabilized zirconia with same overall thickness (between 60 and 70 nm) and different number of interfaces (from 1 up to 9) have been deposited on MgO(110) and the role of the residual compressive strain on the electrical properties has been investigated by means of XRD analysis and impedance spectroscopy. The results, showing no effect of the strain field on the ionic conductivity, indicate the negligible effect of the compressive strain on the ionic transport properties of the material.

Received 18th May 2018,
Accepted 10th July 2018

DOI: 10.1039/c8cp03166e

rsc.li/pccp

Introduction

Ionically conductive interfaces can have properties substantially different from the starting bulk materials, as demonstrated by many examples in the literature.¹ Both grain boundaries and heterogeneous interfaces have a significant influence on the ionic conduction of the materials. In this context thin films are particularly useful to investigate boundaries and interfaces, since they allow for the investigation of properties not easily accessible in ceramics.^{1,2}

The effect of the grain boundaries on the ionic conduction has been extensively studied in fluorite-structured materials with low dopant content, *e.g.* Gd-doped ceria and yttria stabilized zirconia (YSZ) both thin film and ceramic.^{3–7} Even if the amount of impurities such as silica is minimized, the grain boundaries of these materials hinder the ionic conduction with respect to the bulk, due to space charge effects occurring as a consequence of an excess positive charge in the grain boundary core.⁸ It has recently been reported how the grain boundaries conductivity is strongly affected by the solute concentration, while the effect of the structural character is less relevant; in calcium doped CeO₂ for instance the grain boundary conductivity increases of two orders or magnitude increasing the solute concentration to 40 mol%.⁹

In highly doped materials instead, the effect of the grain boundaries on the ionic transport has not been so largely

characterized. Generally the increase of doping content above the optimal value (5 mol% Gd₂O₃-doped CeO₂ and 8 mol% Y₂O₃-doped ZrO₂) leads to a decrement of the ionic conductivity and increment of the activation energy in the bulk of the materials, due to the reduced mobility of oxygen vacancies.^{10,11} Moreover, in the case of high dopant concentration the approximation of a dilute solution is not valid anymore and the space charge model generally used cannot be applied. This was also noticed in various studies which reported disagreement between the calculated and observed extension of the accumulation/depletion layer.^{12–14} A novel and more inclusive approach was presented in the last years which combines the classic Poisson–Boltzmann with the Hillard–Cahn model.¹⁵

In the case of heterointerfaces such as the ones in multilayers of different alternated oxides, various effects can contribute to modify the ionic transport properties of the materials, *i.e.* strain effect^{16,17} or space charge effect.^{18,19}

The impact of strain effect has attracted much attention in the past years. Strain in thin films is known to have a significant effect on the ionic transport properties of materials according to thermodynamics considerations,^{20,21} which relate a tensile strain to a beneficial effect on the ionic conductivity while, on the contrary, a compressive strain leads to a decreased ionic transport.^{22–25} According to DFT simulations, possible cations segregation at the film interface can counterbalance the diminished migration barrier at interfaces under tensile strain, while for compressive strain the migration barriers is increased.²⁶ In the literature are reported mostly studies on the effect of tensile strain on the ionic conductivity, in particular on YSZ and GDC, whose outcomes are somewhat erratic.^{27,28}

Max Planck Institute for Solid State Research, Stuttgart, Germany.

E-mail: elisa.gilardi@psi.ch

† Present address: Laboratory for Multiscale Materials Experiments, Paul Scherrer Institut, 5232 Villigen, Switzerland.



For example the system of multilayers of YSZ/ Sc_2O_3 , YSZ/ LuO_3 and YSZ/ Y_2O_3 studied by Korte *et al.*²² showed an improvement of the conductivity resulting from the variation of the mismatch from compressive to tensile. A similar effect has been observed in YSZ/ $\text{Gd}_2\text{Zr}_2\text{O}_7$ multilayers, with an increased ionic conductivity attributed to the tensely strained YSZ layer.²⁹ More recently, further studies pointed out instead the marginal effects of the lattice tensile strain on the ionic transport of epitaxial multilayers of CeO_2 /8YSZ and GDC single layers.^{30,31} Investigations on the role of compressive strain are rather limited. Moreover, as pointed out by Shen *et al.*,³² particular attention has to be addressed to the actual residual strain in the sample, which is not only dependent on the lattice mismatch between the layers but also on the thickness of the sample, and on the possible formation of dislocations as well as other structural modifications occurring at the interface between film and substrate or between single layers in a multilayered sample. These effects can overlap and a detailed study is required to extrapolate the single contributions to the overall transport properties.

In this context, in order to investigate the ionic transport properties of a highly doped material and its dependence on the microstructure, we studied $\text{Y}_2\text{Zr}_2\text{O}_7$ single layers grown on different substrates (MgO , Al_2O_3) and, in order to address to the effect of strain, multilayers of $\text{Y}_2\text{Zr}_2\text{O}_7$ and 8 mol% - yttria stabilized zirconia (8YSZ) have been investigated.

We note that oxides with the general formula $\text{A}_2\text{B}_2\text{O}_7$ encompass both the defective fluorite and pyrochlore structure. These structures are closely related, but, while in the first one cations and oxygen vacancies are randomly distributed as in a highly doped fluorite, in the pyrochlore structure all atoms occupy specific lattice positions.^{33,34} The ratio between the ionic radii of cations seems to be a key parameter for determining the crystallographic structure of the compound.³⁵ In the case of $\text{Y}_2\text{Zr}_2\text{O}_7$, the defective fluorite structure prevails and hence such an oxide can be treated as a highly doped yttria stabilized zirconia.

Experimental

$\text{Y}_2\text{Zr}_2\text{O}_7$ oxide powder was prepared starting from $\text{ZrO}(\text{NO}_3)_2$ hydrate (Sigma Aldrich 99.99%) and $\text{Y}(\text{NO}_3)_3$ hydrate (Alpha Aesar 99.99%). The exact amount of water in the powder was determined by thermogravimetry analysis. The reactants were heated in synthetic air (20% O_2 + 80% N_2) up to 800 °C with a heating rate of 5 °C min^{-1} . This analysis allowed also for identifying the suitable temperature for the calcination process to remove the glycerol (see below).

The final oxide powder was obtained by heating and combusting the water solution of the two nitrates and 5% v/v of glycerol followed by calcination at 800 °C for 5 hours. Chemical analyses on the powder have been performed by inductively coupled plasma optical emission spectrometry (ICP-OES, Ciroso Spectro Analytical Instruments GmbH).

Ceramic pellets used for the conductivity measurements were uniaxially pressed at 450 MPa and sintered in air at 1700 °C for 10 hours. The density after sintering was 4.00 g cm^{-3} calculated

with geometrical method (relative density 73%). The target for the pulsed laser deposition was pressed uniaxially (160 MPa) and sintered at 1700 °C for 10 hours in air.

Thin films were grown by PLD, using an excimer laser with wavelength of 248 nm (Coherent GmbH, Germany) on different substrates ($\text{MgO}(110)$, $\text{Al}_2\text{O}_3(0001)$, $\text{Al}_2\text{O}_3(1\bar{1}02)$) of size 10 × 10 × 0.5 mm^3 (Crystec GmbH) using the same parameters published elsewhere.³⁶ The energy density on the target was 1.5 J cm^{-2} , with a pulse frequency of 5 Hz. The distance between target and substrate was 43 mm. During the film deposition the oxygen atmosphere was kept at 0.001 mbar and the temperature at 660 °C (measured on the surface of the substrate with a pyrometer by Heimann optoelectronics model KT19.99). After deposition the samples were annealed in pure oxygen ($p\text{O}_2 = 1$ bar) at the deposition temperature for 30 minutes. Multilayers of $\text{Y}_2\text{Zr}_2\text{O}_7$ (lattice parameter, $a = 5.23$ Å) and 8 mol% yttria-doped zirconia (YSZ) (lattice parameter, $a = 5.14$ Å) were prepared using the same deposition conditions with a laser fluency of 3 J cm^{-2} .

For the X-ray diffraction (XRD) analysis a Bruker D8 Diffractometer (Cu-K_α radiation, wavelength of 1.5418 Å) was employed. The texture of the thin films was investigated using XRD pole figures analysis performed with a Philips X'Pert XRD diffractometer (Co-K_α radiation, wavelength of 1.78897 Å). The φ and ψ scan were recorded for 2 defined 2θ angles, namely at 40.50° and 69.0°. The software Carine 3.1 was employed to predict the peaks position of the selected plane along the angle ψ and their multiplicity.

Reciprocal space maps on single layers and multilayers were obtained employing a PANalytical Empyrean diffractometer.

Two different electrode configurations have been used in this study to characterize the electrical transport properties: (i) two planar platinum electrodes (about 400 nm thick and $4.5 \times 10 \text{ mm}^2$ large) sputtered on the top of the films, or (ii) two vertical platinum electrodes (perpendicular to the substrate), which were deposited after having etched off part the films down to the substrate by argon ion milling (Roth and Rau Unilab etching machine) as illustrated in Fig. 1.

The electrical properties were measured using an impedance spectrometer (Novocontrol Alpha-A High Performance Frequency Analyzer) operated at frequencies ranging between 2 MHz and 0.02 Hz by applying an A.C. voltage of 0.1 V. Impedance spectra were collected under oxidizing atmosphere; the $p\text{O}_2$ was monitored by a commercial oxygen sensor (Rapidox 2100, Cambridge Sensotec). The resulting spectra were analyzed with the software Zview2 (Scribner Associates, Inc.).

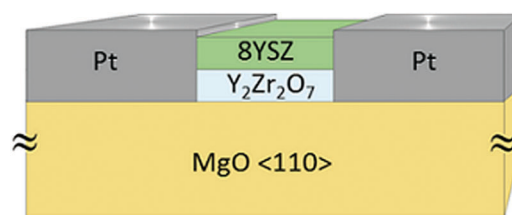


Fig. 1 Illustration of the electrodes used to characterize the conductivity of multilayers of YSZ and $\text{Y}_2\text{Zr}_2\text{O}_7$.



The impedance spectra used for the determination of the electrical transport properties were acquired upon equilibration up to 40 hours at 500 °C and 8 hours at 700 °C at constant oxygen partial pressure while multilayers were exposed to a maximum temperature of 600 °C. For the analysis of EIS spectra of thin films, the capacitance of the films was not considered, since the parasitic capacitance deriving from the measurement set up and from the substrate typically overshadows the film capacitance. Therefore, for the calculation of the electrical conductivity only the resistance determined by the spectra fit was used.

Results and discussion

Structural characterization

Single films of various thicknesses were deposited on $\text{Al}_2\text{O}_3(0001)$, $\text{Al}_2\text{O}_3(1\bar{1}02)$ and $\text{MgO}(110)$ while heterostructures consisting of alternating $\text{YSZ}/\text{Y}_2\text{Zr}_2\text{O}_7$ layers were grown on $\text{MgO}(110)$ only. The XRD patterns (Fig. 2a and b) show that $\text{Y}_2\text{Zr}_2\text{O}_7$ films are mainly oriented along the (111) direction on $\text{Al}_2\text{O}_3(1\bar{1}02)$ as well as on $\text{Al}_2\text{O}_3(0001)$. Peaks from the sample holder were not always present in the measurement and were dependent on the offset used. XRD patterns of thin film grown on $\text{Al}_2\text{O}_3(1\bar{1}02)$ were acquired after deposition of the electrodes, therefore also peaks stemming from platinum electrodes are visible.

In some samples a second weak peak corresponding to the (200) orientation has been observed. For the samples grown on $\text{MgO}(110)$ (Fig. 2c) only the orientation (220) can be detected while the corresponding pole figures exhibit only two peaks at

$\psi = 45^\circ$, indicating perfectly epitaxial thin films (Fig. 3a). It is interesting to note that the films grown on the alumina substrates exhibit peaks belonging to two different orientations despite their smaller mismatch compared to $\text{MgO}(110)$ (ranging between 10% and 15% on the two different Al_2O_3 substrates and amounting -23% on MgO). The result is consistent with the pole figures measurement, where the two distributed intensity along the ϕ axis, at $\psi = 54^\circ$, indicate a textured in-plane alignment of the grains (Fig. 3b). The peaks are repeated every 120° along ϕ according to the threefold symmetry of the (111) plane. The intensity at $\psi = 38^\circ$ instead does not originate from the $\text{Y}_2\text{Zr}_2\text{O}_7$ phase but from the (104) plane of the substrate. The less intense signals visible in the pole figures are instead attributed to the background. AFM analysis of the film surfaces (not shown here) allowed for the determination of a very low surface roughness, comparable to the size of a unit cell for both the textured and the epitaxial samples (4.65–5.21 Å).

As far as the heterostructures are regarded, the XRD analysis (Fig. 4) reveals two peaks for the bilayer, while for the other heterostructures, the peaks are split in first order satellites peaks (labelled as SL_1 and SL_{-1}), which results from interference effects due to the high density of interfaces. As the angular spacing of the satellites peaks depends on the thickness of the layers referring for both the YSZ and $\text{Y}_2\text{Zr}_2\text{O}_7$ layers to the same order peak, one can write³⁷

$$A = \frac{\lambda_{\text{Cu}}}{(\sin \theta_1 - \sin \theta_2)} \quad (1)$$

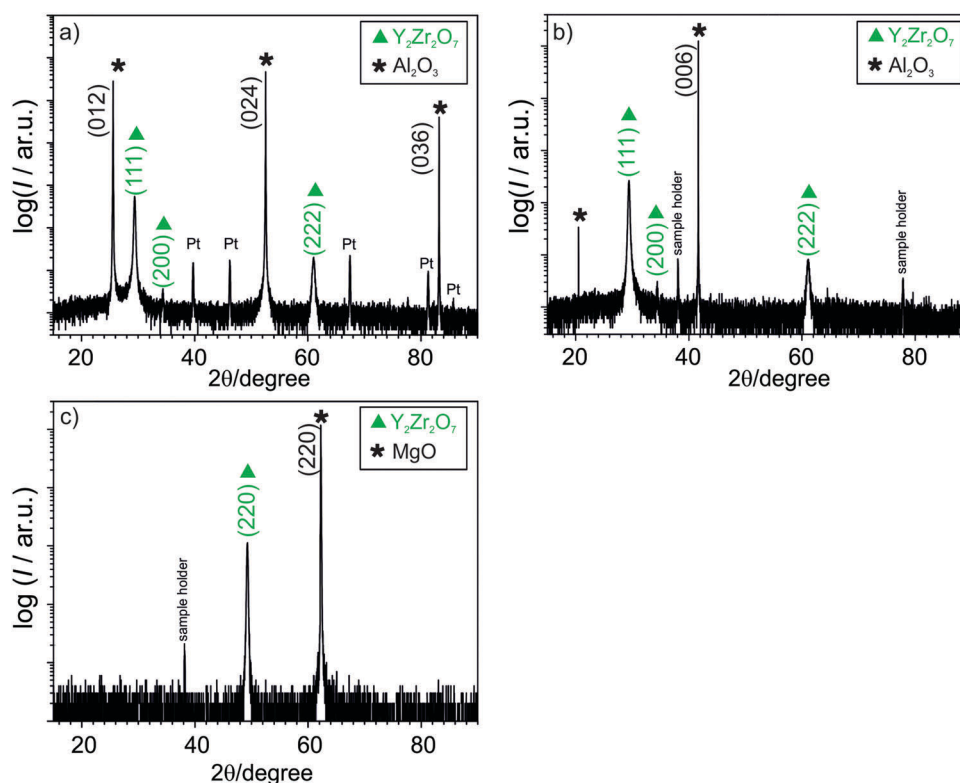


Fig. 2 XRD patterns of $\text{Y}_2\text{Zr}_2\text{O}_7$ thin films grown on (a) $\text{Al}_2\text{O}_3(1\bar{1}02)$, (b) $\text{Al}_2\text{O}_3(0001)$, (c) $\text{MgO}(110)$.



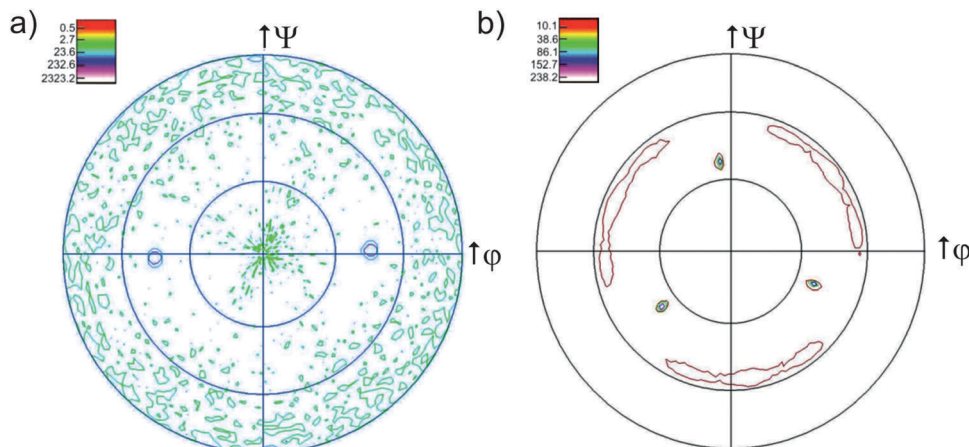


Fig. 3 {001} Pole figure ($2\theta_{\text{Co-K}\alpha} = 40.5^\circ$) of (a) epitaxial thin film on MgO(110). (b) A textured thin film grown on $\text{Al}_2\text{O}_3(0001)$: the distributed intensity along φ indicates the partially textured microstructure of the sample.

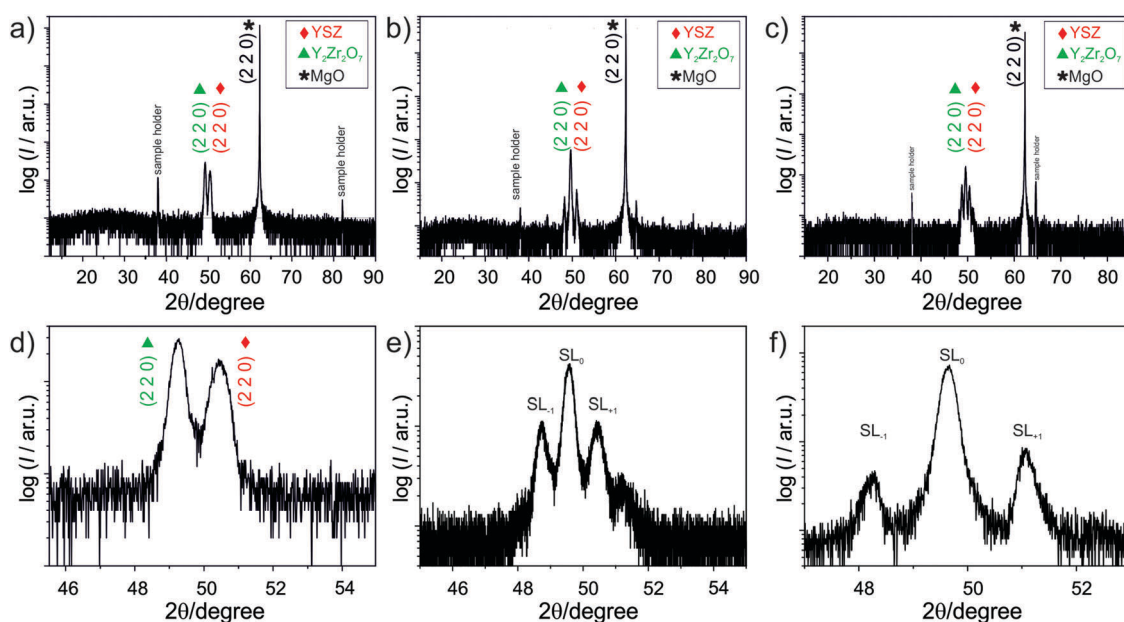


Fig. 4 XRD patterns of YSZ/ $\text{Y}_2\text{Zr}_2\text{O}_7$ epitaxial heterostructures on MgO(110) having roughly the same overall thickness but different number of interfaces: 1 for (a), 5 for (b) and 10 for (c). In panels (d)–(f) the magnification of the corresponding reflections showing the additional peaks due to the interfaces are displayed. The satellites peaks SL_1 and SL_{-1} allow for the calculation of the constituting unit (a single pair of YSZ and $\text{Y}_2\text{Zr}_2\text{O}_7$ layers) thickness: 11.8 nm from (e) ($5 \times (10 \text{ nm} - 10 \text{ nm})$) and 6.8 nm from (f) ($10 \times (5 \text{ nm} - 5 \text{ nm})$).

where λ is the thickness of the constituting $\text{Y}_2\text{Zr}_2\text{O}_7/\text{YSZ}$ unit, λ_{Cu} the radiation wavelength (here the Cu $\text{K}\alpha$ radiation), θ_1 and θ_2 denote the angular spacing of the satellite peaks obtained from the XRD patterns. The position of the satellite peaks have been calculated by fitting the experimental data with a Pearson type VII distribution function.³⁸ The effective real thickness of the layers obtained from the XRD patterns are 11.8 nm for the 5 interfaces sample (indicated as $5 \times (10 + 10)$) and 6.8 nm for the 10 interfaces sample ($10 \times (5 + 5)$). Therefore, the total thickness is estimated to be about 60 nm for the $5 \times (10 + 10)$ multilayer and about 70 nm for the $10 \times (5 + 5)$. Although the total thickness of the bilayer sample could not be directly calculated from the XRD data due to the obvious lack of

interfaces, we could estimate it from the number of deposition pulses and the growth rate of the two oxides to be about 60 nm.

Reciprocal space maps on single layers and multilayers were obtained around the YSZ(331), (33 $\bar{1}$), (420) and (240) reflections (Fig. 5). The in plane and out of plane momentum transfers can be separated considering that the reflection (420) is constituted by the sum of the vectors (330) and (1 $\bar{1}$ 0); while the (331) is the sum of (330) and (001) vectors.

In Fig. 5a and b are shown the reciprocal space maps around the reflections (33 $\bar{1}$), of a single layer of $\text{Y}_2\text{Zr}_2\text{O}_7$ (70 nm thickness) and a single layer (60 nm thickness) of YSZ respectively, all grown epitaxially on MgO(110). The elongated shape of peak along the in plane momentum transfer direction is related to



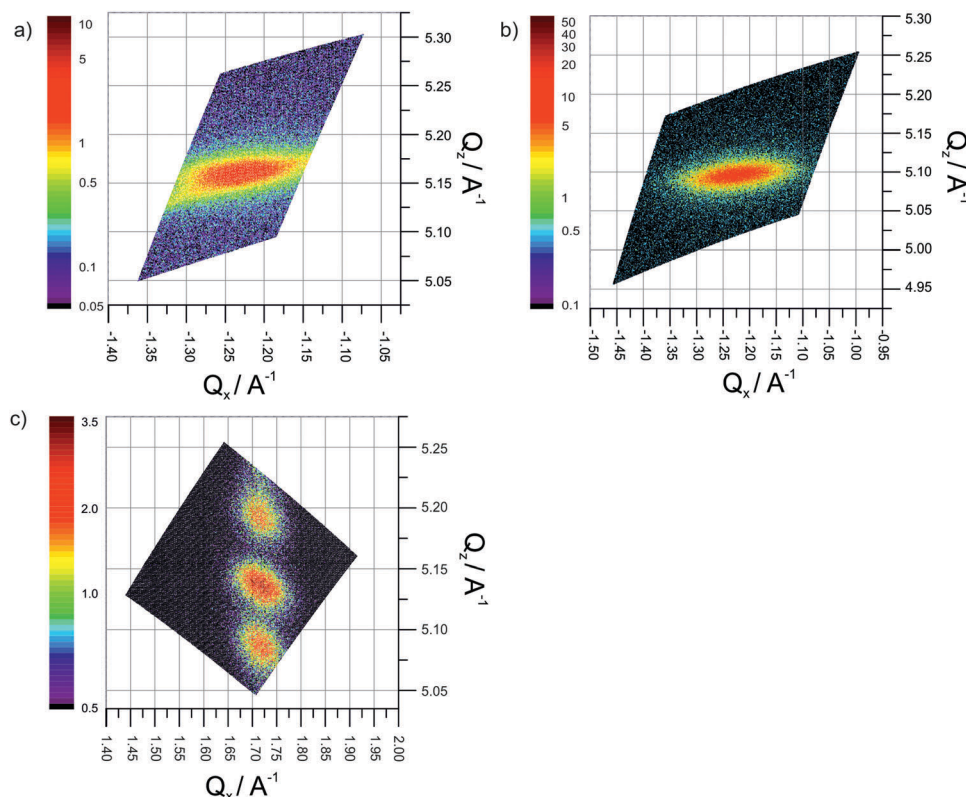


Fig. 5 Reciprocal space maps around the (33-1) reflection of (a) single layer of $\text{Y}_2\text{Zr}_2\text{O}_7$, (b) single layer of YSZ. Reciprocal space map around the (420) reflection of a multilayer $5 \times (10 \text{ nm} + 10 \text{ nm})$, which were all grown epitaxially on $\text{MgO}(110)$. Q_x and Q_z indicate the in plane and out of plane momentum transfer respectively. Color indicates the intensity (in arbitrary units). The intensity is reported in logarithmic scale in (a) and (b) and in linear scale in (c).

the presence of defects in the sample. Since the TEM analysis (reported in ref. 36 for a $\text{Y}_2\text{Zr}_2\text{O}_7$ single layer) confirmed the absence of grain boundaries or mosaic microstructure, such effect is attributed to the high density of misfit dislocations at the interface.

Both the in-plane Q_x and out-of-plane Q_z momentum transfers show an almost complete relaxation of the strain deriving from the mismatch with the substrate. Notably, for the YSZ thin film, the comparison with the values of interplanar distance reported in literature (ICDD: 01-082-1246) reveal an out-of-plane value along the [110] direction of +0.5%, while in plane an average (compressive) strain of -0.9% is found. Such an outcome is qualitatively expected since it corresponds to the situation, according to which the substrate $\text{MgO}(110)$ having a smaller lattice parameter keeps the film under in-plane compressive strain. Such an in-plane compression demands an expansion in the perpendicular direction in agreement with expected Poisson ratio.

A similar situation (although to a different extent) holds also for the $\text{Y}_2\text{Zr}_2\text{O}_7$ thin film. Here, the in-plane compressive strain is equal to -0.4%, while along out-of-plane direction the strain is 0.3%.

The reciprocal space map around the (420) reflection of the $5 \times (10 \text{ nm} + 10 \text{ nm})$ multilayer (Fig. 5c) clearly exhibits satellite peaks stemming from the periodicity of the system. In this case, it is not possible to separate YSZ and $\text{Y}_2\text{Zr}_2\text{O}_7$ in-plane

contributions, due to the very similar lattice parameters of the two materials. Nonetheless, the out-of-plane lattice parameters could be estimated by simulating the intensity profile of a stack of $([\text{YSZ}]_{20}[\text{YZO}]_{20})_5$. This indicates an out-of-plane lattice expansion of +0.4% suggesting that also the multilayers are kept under in-plane compressive strain by the substrate as observed in the single layers.

Also in this case the broadening of the peaks can be attributed to a high density of extended defects perpendicular to the interface, most likely misfit dislocations at the interface to the substrate. In this context, the Scherrer's formula cannot be directly used to calculate the average distance between the dislocations since the peak broadening depends also on the intensity of the Burgers' vector of the dislocation and the relative orientation of between the Burgers vector and line dislocation.³⁹ Nevertheless the difference in the peak broadening between the single layers suggests a different density of misfit dislocation in the samples. In particular, it indicates a larger misfit density in the single layer of YSZ compared to the $\text{Y}_2\text{Zr}_2\text{O}_7$ single layer and the multilayers.

Electrical measurements

Single films. Let us first consider the electrical transport properties of the pellet. As shown in Fig. 6a only one contribution stemming from the sample can be recognized in the impedance Nyquist plot and therefore the impedance spectra



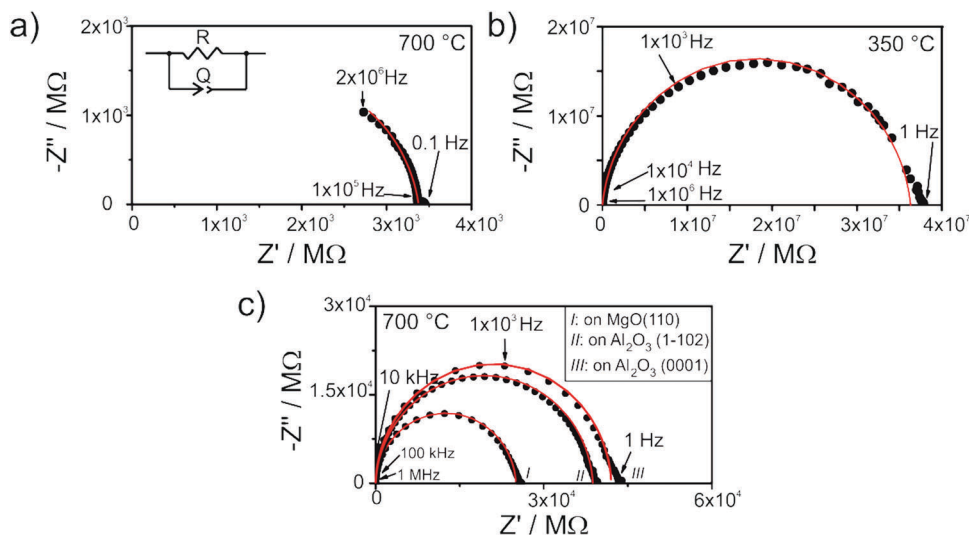


Fig. 6 Impedance Nyquist plot of (a) a microcrystalline pellet acquired in oxygen at 700 °C (b) of the same sample at 350 °C, (c) of thin films 100 nm thick grown on different. The symbols correspond to the experimental data while the continuous lines result from fitting the spectra using the equivalent circuit in the inset of (a).

are fitted using an equivalent circuit consisting of an electrical resistance in parallel with a constant phase element Q , which is defined as $C = (R^{1-n}Q^n)^{1/n}$ with C being the capacitance, R the resistance and n an additional fitting parameter. The second contribution is instead stemming from the electrode. In the light of the resulting relative permittivity ($C = 8.4 \times 10^{-12}$ F and $\epsilon_r \sim 30$) this contribution can be attributed to the bulk behavior indicating that within the whole temperature range the grain boundaries seem not to hinder the ionic transport (oxygen vacancies).

Also the spectra acquired from the single thin films (Fig. 6b and c) exhibit only one semicircle. This is expected as, owing to the experimental setup configuration, the resulting stray capacitance exceeds the bulk and grain boundary capacitances by orders of magnitude.⁴⁰ For this reason, it is not possible to distinguish bulk from grain boundary contribution, and the impedance spectra are fitted using the same equivalent circuit as the one shown above.

The resulting electrical conductivity and activation energy data are summarized in Fig. 7 and Table 1. It is evident that not only textured and epitaxial films (Fig. 7a) but also epitaxial and polycrystalline samples (Fig. 7b) exhibit very similar electrical conduction properties suggesting that the microstructure (*i.e.* the presence of grain boundaries) only marginally affects the ionic transport. It is worth comparing these results with literature data obtained from YSZ thin films. For example, Peters *et al.*⁴¹ observed variation of one order of magnitude in the conductivity of $Y_{0.17}Zr_{0.83}O_{1.91}$ thin films (from 10^{-2} S cm⁻¹ to 10^{-3} S cm⁻¹ at 700 °C) by varying the grain size from about 40 nm to 150 nm in 400 nm thick layers deposited by sol-gel method. Similarly, Schlupp *et al.*⁴² measured a conductivity decrease of more than 1 order of magnitude (from 8×10^{-5} S cm⁻¹ to 1×10^{-6} S cm⁻¹ at 400 °C), together with an activation energy increase of 0.3 eV when comprising columnar grown with

nanocrystalline thin films of 8YSZ deposited *via* chemical vapor deposition.

These results allow one to conclude that compared to a parent system (8YSZ), the grain boundaries in $Y_2Zr_2O_7$ do not hinder the oxygen vacancy transport. To the best of our knowledge there are no studies about grain boundary contribution to the ionic conductivity in zirconate pyrochlores or defective fluorite thin films in the literature whereas a markedly blocking effect of the grain boundaries has been noticed in pyrochlore ceramics with the composition $(Sm_{1-x}Y_x)_2Zr_2O_7$ with $0 \leq x \leq 0.5$ ⁴³ and $GdSmZr_2O_7$.⁴⁴

We note that as expected for a defective fluorite, both the films and the pellet do not show any conductivity dependence on the oxygen partial pressure in the range between 1 and 10^{-4} atm at 700 °C (*cf.* Fig. 7c and d).

Multilayers. As for the temperature dependence of the conductivity of the multilayers, they are shown in Fig. 8 together with the data acquired from epitaxial single films as reference.

It is noteworthy that the conductivity and activation energy values for the single layer of YSZ are in agreement with literature values: Joo *et al.*⁴⁵ reported a conductivity of 3×10^{-3} S cm⁻¹ at 600 °C, in this work the measured conductivity is 2.9×10^{-3} S cm⁻¹ and an activation energy of 1.01 eV for a YSZ PLD-film of 0.6 μ m thickness.

In absence of interface effects (*e.g.* space-charge or strain), the multilayer systems considered here can be treated as a set of resistances in parallel, each of which corresponding to a single layer. The expected total conductivities can be calculated according to Kirchhoff's law starting from the conductivities of the constituting oxides. In this way, we estimate a conductivity of the multilayers of 1.5×10^{-3} S cm⁻¹ at 600 °C.

The actual experimental values measured at 600 °C are: 1.7×10^{-3} S cm⁻¹ for the $10 \times (5-5)$ multilayer, 1.5×10^{-3} S cm⁻¹ for the $5 \times (10-10)$ multilayer and 1.8×10^{-3} S cm⁻¹ for the bilayer.



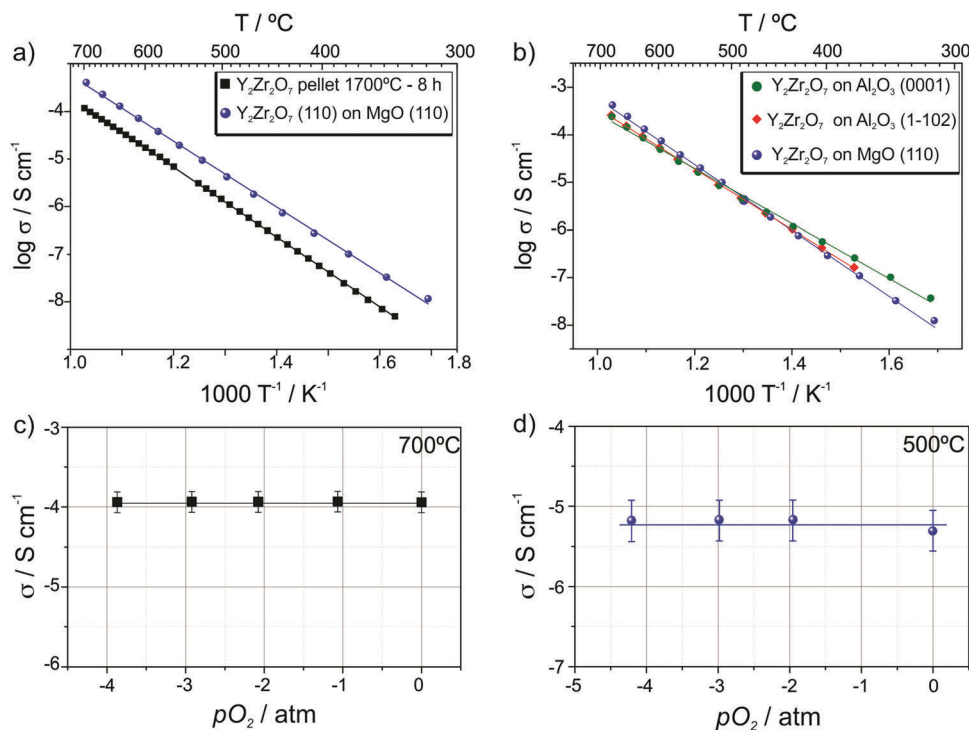


Fig. 7 Temperature dependence and activation energy of (a) $\text{Y}_2\text{Zr}_2\text{O}_7$ pellet compared with an epitaxial thin film grown on MgO, (b) $\text{Y}_2\text{Zr}_2\text{O}_7$ thin films on different substrates, MgO and Al_2O_3 , constant thickness 100 nm. $p\text{O}_2$ dependence of the conductivity of (c) a ceramic pellet and (d) of an epitaxial thin film on MgO.

Table 1 Activation energy and conductivity of thin films of $\text{Y}_2\text{Zr}_2\text{O}_7$ (thickness 100 nm) deposited on different substrates

$\text{Y}_2\text{Zr}_2\text{O}_7$ sample	Activation energy/eV	σ at 700 °C/S cm ⁻¹
On MgO(110) epitaxial	1.44 ± 0.01	4.01×10^{-4}
On Al_2O_3 (0001) textured	1.26 ± 0.01	2.37×10^{-4}
On Al_2O_3 (1102) textured	1.32 ± 0.01	2.58×10^{-4}
Pellet	1.52 ± 0.002	1.17×10^{-4}

Such a small difference between the expected and the measured values indicates that the conductivity of the heterolayers is neither varied by the number of interfaces nor by the different thicknesses of the single constituting layers, meaning that neither space charge nor strain effects modify the ion transport properties compared to the bulk situation. Consistently, also the values of the activation energy vary only marginally (from 1.08 eV for the bilayer to 1.10 eV for the $5 \times (10-10)$ and 1.14 eV for the $10 \times (5-5)$ samples).

From thermodynamic considerations, it has been calculated that the strain alters the ionic transport and its effect is proportional to the mismatch between layers (this is strictly valid only for epitaxial systems).²⁷ Here, however we recognize that even in perfectly epitaxial systems with high quality of the interfaces (confirmed by XRD analysis) below the critical thickness, where the strain is not released through one-dimensional or two-dimensional defects, the substantial residual strain field (compressive in-plane and tensile out-of-plane) does not result in any perceptible variation of the oxygen ion transport.

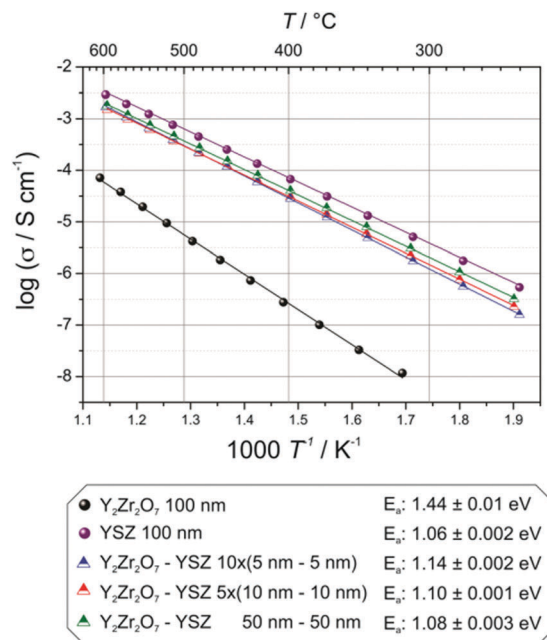


Fig. 8 Temperature dependence of the conductivity of YSZ- $\text{Y}_2\text{Zr}_2\text{O}_7$ multilayers with different number of interfaces. For comparison also the data of single layers of YSZ and $\text{Y}_2\text{Zr}_2\text{O}_7$ are displayed.

To the best of our knowledge, there are no theoretical studies in literature on the effect of compressive strain on the ionic conductivity of YSZ. Nonetheless if we refer to studies on



the effect of tensile strain on the ionic transport of YSZ (as the work by Kushima and Yildiz²⁵) and assume a symmetric effect in the case of a compressive strain, our results are in qualitative agreement with the literature. The authors reported an increasing effect of the strain on the hopping barrier of oxygen vacancies up to a strain of 4% with such an effect being more pronounced at lower temperatures. It is worth noticing that, not only the trend of an increasing effect on the activation energies with increasing strain is in agreement with our observation, but also the variation of the activation energy (calculated for less than 1% strain) being close to 0.1 eV is consistent with our experimental findings.

For the sake of completeness, we note that our results are however not in line with the observations of Li *et al.*,²⁹ who detected a different behavior for their multilayered Gd₂Zr₂O₇ and YSZ heterostructures grown on Al₂O₃ with a variable number of interfaces. In that study, the authors measured a substantial variation of the ionic conductivity (an increase of 2 orders of magnitude when moving from 10 to 20 interfaces) for a lattice mismatch of about 3%, while no information was given on the activation energy. It is arduous to rationalize such a discrepancy, since it might well depend on different procedures of the sample preparation that might lead to nominally similar samples but having different microstructures and/or strain situations. In this work, we took carefully into account the microstructure and real residual strain of the multilayers, observing that secondary effects stemming from grain boundaries and misfit dislocations can be excluded to be present in our multilayered samples.

Conclusions

Y₂Zr₂O₇ thin films have been successfully grown on various substrates (MgO(110), Al₂O₃(0001), Al₂O₃(1102)) by pulsed laser deposition. The study of their electrical properties (impedance spectroscopy) at different temperatures and oxygen partial pressure shows that these are only marginally affected by their orientation and microstructure, since the ionic conductivity variation amounts only a factor two between epitaxial (on MgO(110)) and polycrystalline thin films (on Al₂O₃(0001) and Al₂O₃(1102)).

Heterolayers of YSZ/Y₂Zr₂O₇ with different number of interfaces were characterized to investigate the role of strain on the ionic conductivity of YSZ. A combined study relying on the determination of the residual strain field in the multilayers and on the evaluation of their ionic transport properties did not reveal any perceptible effect of strain on the oxygen vacancy transport. Such a finding may be interpreted in term of a mutually compensating effect between the deleterious compressive in-plane strain and the beneficial tensile out-of-plane strain resulting from the substrate MgO(110) with a smaller lattice constant compared to YSZ and Y₂Zr₂O₇.

Author contributions

The manuscript was written through contributions of all authors. All authors have given approval to the final version of the manuscript.

Conflicts of interest

There are no conflicts to declare.

Acknowledgements

The authors wish to thank G. Christiani and B. Stuhlhofer for their technical support for pulsed laser deposition. R. Merkle is thanked for helpful discussions. M. Dudek is thanked for the pole figure acquisition. H. Boschker is thanked for the RSM characterization. Fig. 2c, 3a, and 7a were adapted with permission from (*ACS Appl. Mater. Interfaces*, 9(32), 27257–27265). Copyright (2017) American Chemical Society. Open Access funding provided by the Max Planck Society.

References

- 1 E. Fabbri, D. Pergolesi and E. Traversa, *Sci. Technol. Adv. Mater.*, 2010, **11**, 054503.
- 2 X. Guo and J. Maier, *Adv. Mater.*, 2009, **21**, 2619–2631.
- 3 X. Guo and J. Maier, *J. Electrochem. Soc.*, 2001, **148**, E121–E126.
- 4 C. Peters, A. Weber, B. Butz, D. Gerthsen and E. Ivers-Tiffée, *J. Am. Ceram. Soc.*, 2009, **92**, 2017–2024.
- 5 M. C. Gobel, G. Gregori and J. Maier, *Phys. Chem. Chem. Phys.*, 2011, **13**, 10940–10945.
- 6 S. Kim, J. Fleig and J. Maier, *Phys. Chem. Chem. Phys.*, 2003, **5**, 2268–2273.
- 7 Y. M. Chiang, E. B. Lavik, I. Kosacki, H. L. Tuller and J. Y. Ying, *Appl. Phys. Lett.*, 1996, **69**, 185–187.
- 8 X. Guo and R. Waser, *Prog. Mater. Sci.*, 2006, **51**, 151–210.
- 9 W. J. Bowman, M. N. Kelly, G. S. Rohrer, C. A. Hernandez and P. A. Crozier, *Nanoscale*, 2017, **9**, 17293–17302.
- 10 C. T. Chen, S. Sen and S. Kim, *Chem. Mater.*, 2012, **24**, 3604–3609.
- 11 J. T. S. Irvine, I. R. Gibson and D. P. Fagg, *Ionics*, 1995, **1**, 279–285.
- 12 N. Shibata, F. Oba, T. Yamamoto, Y. Ikuhara and T. Sakuma, *Philos. Mag. Lett.*, 2002, **82**, 393–400.
- 13 H. B. Lee, F. B. Prinz and W. Cai, *Acta Mater.*, 2013, **61**, 3872–3887.
- 14 M. C. Gobel, G. Gregori and J. Maier, *Phys. Chem. Chem. Phys.*, 2014, **16**, 10214–10231.
- 15 D. S. Mebane and R. A. De Souza, *Energy Environ. Sci.*, 2015, **8**, 2935–2940.
- 16 J. L. M. Rupp, *Solid State Ionics*, 2012, **207**, 1–13.
- 17 N. Schichtel, C. Korte, D. Hesse and J. Janek, *Phys. Chem. Chem. Phys.*, 2009, **11**, 3043–3048.
- 18 N. Sata, K. Eberman, K. Eberl and J. Maier, *Nature*, 2000, **408**, 946–949.
- 19 G. Xiangxin, I. Matei, J. Jamnik, L. Jong-Sook and J. Maier, *Phys. Rev. B: Condens. Matter Mater. Phys.*, 2007, **76**, 1–7.
- 20 R. A. De Souza, A. Ramadan and S. Horner, *Energy Environ. Sci.*, 2012, **5**, 5445–5453.
- 21 A. P. C. Korte, J. Janek, D. Hesse and N. Zakharovb, *Phys. Chem. Chem. Phys.*, 2008, **10**, 4623–4635.



- 22 C. Korte, N. Schichtel, D. Hesse and J. Janek, *Monatsh. Chem.*, 2009, **140**, 1069–1080.
- 23 J. Hinterberg, T. Zacherle and R. A. De Souza, *Phys. Rev. Lett.*, 2013, **110**, 205901.
- 24 N. Schichtel, C. Korte, D. Hesse, N. Zakharov, B. Butz, D. Gerthsen and J. Janek, *Phys. Chem. Chem. Phys.*, 2010, **12**, 14596–14608.
- 25 A. Kushima and B. Yildiz, *J. Mater. Chem.*, 2010, **20**, 4809–4819.
- 26 D. S. Aidhy, Y. W. Zhang and W. J. Weber, *J. Phys. Chem. C*, 2014, **118**, 4207–4212.
- 27 C. Korte, J. Keppner, A. Peters, N. Schichtel, H. Aydin and J. Janek, *Phys. Chem. Chem. Phys.*, 2014, **16**, 24575–24591.
- 28 B. Yildiz, *MRS Bull.*, 2014, **39**, 147–156.
- 29 B. Li, J. M. Zhang, T. Kaspar, V. Shutthanandan, R. C. Ewing and J. Lian, *Phys. Chem. Chem. Phys.*, 2013, **15**, 1296–1301.
- 30 D. Pergolesi, E. Fabbri, S. N. Cook, V. Roddatis, E. Traversa and J. A. Kilner, *ACS Nano*, 2012, **6**, 10524–10534.
- 31 A. Fluri, D. Pergolesi, V. Roddatis, A. Wokaun and T. Lippert, *Nat. Commun.*, 2016, **7**, 10692.
- 32 W. D. Shen and J. L. Hertz, *J. Mater. Chem. A*, 2015, **3**, 2378–2386.
- 33 L. Minervini, R. W. Grimes and K. E. Sickafus, *J. Am. Ceram. Soc.*, 2000, **83**, 1873–1878.
- 34 B. P. Uberuaga, D. A. Andersson and C. R. Stanek, *Curr. Opin. Solid State Mater. Sci.*, 2013, **17**, 249–256.
- 35 T. Hagiwara, H. Yamamura and H. Nishino, *J. Fuel Cell Sci. Technol.*, 2011, **8**, 1–5.
- 36 E. Gilardi, G. Gregori, Y. Wang, W. Sigle, P. A. van Aken and J. Maier, *ACS Appl. Mater. Interfaces*, 2017, **9**, 27257–27265.
- 37 S. Sanna, V. Esposito, A. Tebano, S. Licoccia, E. Traversa and G. Balestrino, *Small*, 2010, **6**, 1863–1867.
- 38 M. M. Hall, V. G. Veeraraghavan, H. Rubin and P. G. Winchell, *J. Appl. Crystallogr.*, 1977, **10**, 66–68.
- 39 C. C. Tang, *J. Appl. Crystallogr.*, 2007, **40**, 642–649.
- 40 M. Gerstl, E. Navickas, M. Leitgeb, G. Friedbacher, F. Kubel and J. Fleig, *Solid State Ionics*, 2012, **225**, 732–736.
- 41 C. Peters, A. Weber, B. Butz, D. Gerthsen and E. Ivers-Tiffée, *J. Am. Ceram. Soc.*, 2009, **92**, 2017–2024.
- 42 M. V. F. Schlupp, B. Scherrer, H. Ma, J. G. Grolig, J. Martynczuk, M. Prestat and L. J. Gauckler, *Phys. Status Solidi A*, 2012, **209**, 1414–1422.
- 43 X. L. Xia, J. H. Ouyang, Z. G. Liu, S. A. Gao and S. Li, *J. Electrochem. Soc.*, 2010, **157**, B470–B476.
- 44 Z. G. Liu, J. H. Ouyang, K. N. Sun and Y. Zhou, *J. Power Sources*, 2012, **210**, 96–100.
- 45 J. H. Joo and G. M. Choi, *Solid State Ionics*, 2006, **177**, 1053–1057.

